GDCh Research Article Angewandte International Edition Chemie www.angewandte.org

How to cite: *Angew. Chem. Int. Ed.* **2025**, *64*, e202508266
doi.org/10.1002/anie.202508266

*Electrochemiluminescence Imaging*

# Single-Molecule Electrochemiluminescence Imaging of Plasmonic Hot Spot Reactivity

*Xuedong Huang, Qian Shi, Yanwei Lu, Binxiao Li, Yujun Ning, Langxia Feng, Neso Sojic,* Dechen Jiang,* and Baohong Liu**

**Abstract:** Localized surface plasmon resonance (LSPR), an important optical property of noble metal nanomaterials, is extensively applied in electrochemistry. However, the specific LSPR effects on metallic nanoparticles are difficult to unravel and evaluate, owing to simultaneous factors like intrinsic electroactivity and surface interactions. Herein, we designed a series of shell-isolated nanostructures, with mesoporous silica shells and plasmonic Au Nanorod cores (AuNR@m$SiO_2$), for precisely investigating both LSPR and nanoconfinement effects. Single-molecule electrochemiluminescence (ECL) imaging was employed to monitor the in situ turnover frequency (TOF) of photon emissions on individual plasmonic nanoamplifiers to determine the dominant factors influencing LSPR and nanoconfinement effects. TOF heatmaps and super-resolution ECL images unveiled distinct hot spot distributions along the plasmonic nanostructures. Our approach provides insight into and in-depth understanding of plasmonic effects during electrochemical reactions, thereby facilitating precise electrocatalyst design based on the physiochemical properties of LSPR.

## Introduction

Localized surface plasmon resonance (LSPR), a particular optical property of noble metal materials, draws extensive interest in fields such as catalysis, biosensing, bioimaging, and enhanced optical spectroscopy.[1–4] The local electric field around nanomaterials can be substantially enhanced by incident photons that match the collective oscillation frequency of surface electrons, resulting in optical hot spots and high chemical reaction rates.[5–9] Owing to this intriguing performance, noble metal nanocrystals have assumed an important role in the field of electrochemistry for sensing, energy conversion, and storage functions.[10–12] However, revealing the plasmon-enhanced electrochemistry and obtaining in situ images of hot spots along single plasmonic electrocatalysts remain challenging. Therefore, a high-resolution electrochemical technique needs to be developed to establish the relationship between the morphology and performance of plasmonic electrocatalysts.[13–15]

Electrochemiluminescence (ECL) microscopy, based on sensitive electrochemical reactions and high spatial resolution optical imaging, is a powerful technique that can provide insight into single-molecule reactions on individual plasmonic nanocatalysts.[16–19] Specifically, various noble metal nanocrystals (e.g., Au nanoplates,[20–22] nanoparticles,[23,24] nanodisks,[25] films,[26] as well as bimetallic nanoparticles[27–29]) that exhibit excellent electrochemical performance have been investigated at nanoscale resolution. However, the plasmonic properties of these nano or micromaterials are concealed by their intrinsic electrocatalytic abilities and affected by electron transfer when plasmonic nanoparticles directly contact electrodes. These effects hide the hot spots triggered by LSPR effects during overall ECL enhancement and prevent their clear identification. In addition, plasmonic effect triggered by ECL light is relatively low due to the low efficiency of ECL and is hardly recorded with high spatiotemporal resolution.

Herein, we designed shell-isolated plasmonic nanostructures to completely eliminate the interference from electrochemical reactivity. Subsequently, single-molecule ECL microscopy with high spatiotemporal resolution revealed the reactivity and distribution of plasmonic hot spots on single electrocatalysts. Specifically, Au nanorod (AuNR) cores featuring easily adjustable LSPR properties were coated with mesoporous silica (m$SiO_2$) shells, which avoided the direct electron-transfer reaction between the electrode and the AuNR. This approach allowed to decouple the intrinsic electroactivity of the AuNR from the plasmonic effects. In addition, the mesoporous silica shells helped to maintain the stability of the plasmonic metal surface during electrochemical excitation and offered nanoconfined spaces

[*] X. Huang, Q. Shi, Y. Lu, Dr. B. Li, Y. Ning, L. Feng, Prof. B. Liu
Department of Chemistry, Shanghai Stomatological Hospital, State Key Laboratory of Molecular Engineering of Polymers, Fudan University, Shanghai 200433, P.R. China
E-mail: bhliu@fudan.edu.cn

Prof. N. Sojic
University of Bordeaux, Bordeaux INP, ISM, UMR CNRS 5255, Pessac 33607, France
E-mail: sojic@u-bordeaux.fr

Prof. D. Jiang
State Key Laboratory of Analytical Chemistry for Life and School of Chemistry and Chemical Engineering, Nanjing University, Nanjing, Jiangsu 210093, P.R. China
E-mail: dechenjiang@nju.edu.cn

Additional supporting information can be found online in the Supporting Information section

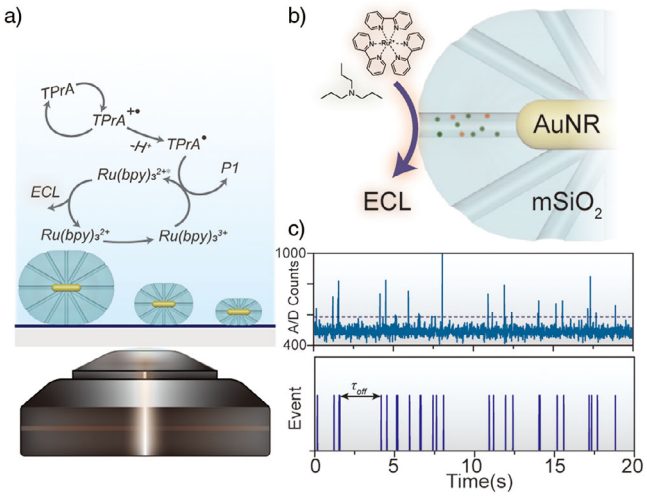


***Figure 1.*** a) Schematic of single-molecule ECL imaging approach for core-shell nanoamplifiers (AuNRs coated with mesoporous silica shells) with different shell thicknesses. P1, iminium cation. b) Illustration of adsorption and ECL reactions in the mesopores of a nanoamplifier. c) Typical analog-to-digital (A/D) counts of a single nanoamplifier and the corresponding single-event burst.

for electrochemical reactions. Bimolecular reaction collisions between the ECL reagents ($Ru(bpy)_3^{2+}$ luminophore and tri-n-propylamine TPrA coreactant) in the nanochannels occurred more frequently under nanoconfinement, resulting in the generation of abundant ECL photons.[30–33] These ECL photons subsequently triggered the oscillation of surface electrons or LSPR effects on the AuNRs. Surface-enhanced ECL occurred through electric field enhancement, upon activation of LSPR, amplifying the ECL signals (Figure 1a,b). Consequently, the ECL signal enhancement due to the nanoconfinement and plasmonic effects of AuNR@$mSiO_2$ was quantitatively characterized and individually analyzed via in situ photon emissions. Additionally, both effects can be analyzed separately by controllable synthesis of the nanoemitters.

## Results and Discussion

Since photon generation in ECL occurred without the assistance of an external light source, the photodetection system could reach near-zero background and realize single-molecule/photon sensitivity (Figure S1A–D).[20,34,35] Under appropriate camera acquisition conditions, the analog-to-digital (A/D) counts of single-pixel displaying individual photon bursts could be transformed into single-event occurrence, as shown in Figures 1c and S1E. Therefore, each single photon represented the optical product of a single electron-transfer reaction resulting from a redox collision, which produced the excited state luminophore. The turnover frequency of photon emission (TOF) could be calculated from the statistical dwell time ($\tau_{off}$) between each single event. In other words, the TOF represented the number of photons emitted by a single nanoamplifier per second andreflected the local ECL reactivity. As shown in Figure S2A–B, while the ECL reagents freely diffused in solution and reacted on the electrode, the average off time ($<\tau_{off}>$) was dependent on the $Ru(bpy)_3^{2+}$ concentration at a constant TPrA concentration. The TOF value (i.e., $<\tau_{off}>^{-1}$) increased along as the $Ru(bpy)_3^{2+}$ concentration increased from 100 nM to 200 μM when excess TPrA (10 mM) was present, finally reaching a plateau. Moreover, the introduction of core-shell nanoamplifiers effectively accelerated the photon generation rate. In detail, nanoamplifiers with identical plasmonic AuNR cores (48 × 12 nm, aspect ratio = 4:1) and diverse $mSiO_2$ thicknesses of shells were synthesized as in previous reports (Figure S3).[36–38] TEM and SEM images revealed that the nanoamplifiers with different shell thickness were in the shape of a cylinder and hemispherical cap (Figures S4–S6). The corresponding $mSiO_2$ shell thicknesses were 60, 42.5, and 27.5 nm (labeled as thick, medium, and thin shells, respectively). Subsequently, AuNR@$mSiO_2$ was deposited onto the electrode surface to achieve single-particle dispersion for photon kinetics analysis (Figures S7–S8).

A burst of ECL intensity was initially measured on a single nanoamplifier, as shown in Figure 2a. Enhancement ECL ratios were calculated by ECL intensity in solution ($I_{solution}$), and on AuNR@$mSiO_2$ nanoamplifier ($I_{particle}$) using the following formula (Equation. 1).

$$\text{Enhancement ECL ratio} = \frac{I_{particle} - I_{background}}{I_{solution} - I_{background}} \quad (1)$$

Enhancement ECL ratios of AuNR@$mSiO_2$ are from 5.5 to 21 with increasing shell thickness. Considering that AuNR@$mSiO_2$ with different shell thicknesses contained similar pore channels (Figure S9), a thicker shell was able to accommodate additional reactant molecules compared to a thinner shell and exhibited a greater nanoconfinement effect. Subsequently, under single photon sensitivity, the TOF values of AuNR@$mSiO_2$ with different thicknesses increased with increasing $Ru(bpy)_3^{2+}$ concentration and exhibited nearly similar trends (Figure 2b). Based on the heterogeneous catalysis of a bimolecular reaction, the ECL reaction of $Ru(bpy)_3^{2+}$ and TPrA in the mesopores was represented by the Langmuir–Hinshelwood (LH) kinetics model, involving mainly the adsorption and desorption of two species.[39,40] Considering one kind of reactant (TPrA) that is at a constant and saturation concentration, TOF curves can be fitted by the simplified LH model (eq. 2).

$$TOF = \frac{kK_A[A]}{1 + K_A[A]} \quad (2)$$

So, the Equation 2 can predict that TOF values will increase with increasing concentration of $Ru(bpy)_3^{2+}$ and finally reach a maximum. By fitting the curve with Equation 2, the reaction kinetics $k$ constant and equilibrium constant $K_A$ of reactant A ($Ru(bpy)_3^{2+}$ in this system) can be calculated. The specific photon emission rate ($k_{eff}$) obtained by the fitting curves provided a quantitative measurement, while the adsorption equilibrium constant ($K_{Ru}$) indicated the change in adsorption environment of the reactant (Table 1).

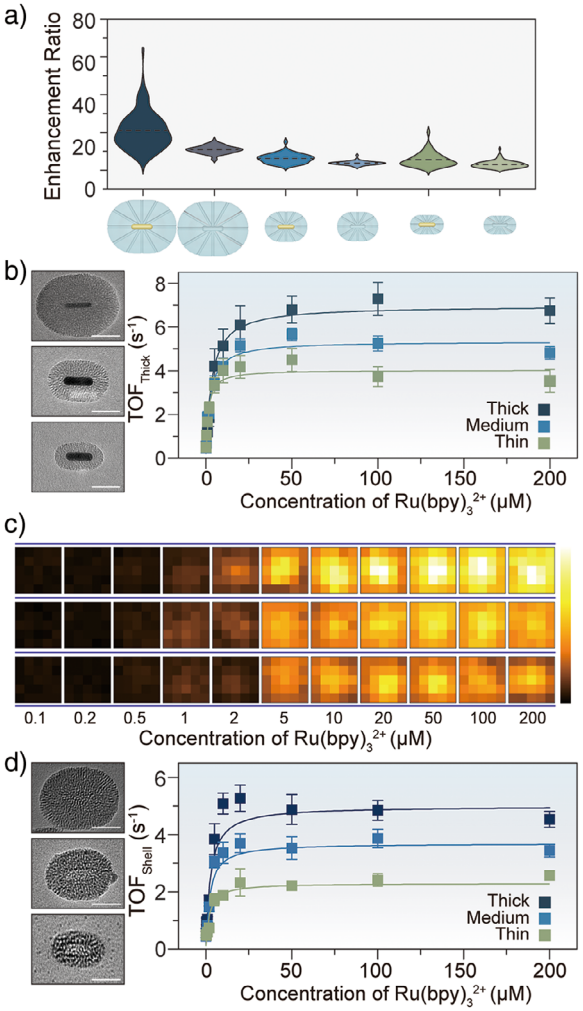


***Figure 2.*** a) Enhancement ECL ratio on AuNR@mSiO$_2$ nanoamplifiers (thick, medium, and thin shells from left to right) and corresponding hollow silica shells. Potential = 1.35 V. b) TEM images and TOF curves of AuNR@mSiO$_2$ nanoamplifiers with three different shell thicknesses. Scale bar: 50 nm. c) Heatmap of sum photons under increasing Ru(bpy)$_3^{2+}$ concentrations (from left to right) on AuNR@mSiO$_2$ nanoamplifiers with three different thicknesses (thick, medium, and thin shells from top to bottom). d) TEM images and TOF curves of hollow silica shells with three different thicknesses. Scale bar: 50 nm. Error bars represent the standard deviation ($n = 20$).

AuNR@mSiO$_2$ with the thickest shell possessed the highest $k_{eff}$ value among the three types, indicating that shell thickness was an important factor in ECL enhancement. As shown by the accumulation of photons in Figure 2c, photon emission mainly occurred at the position of the nanoamplifier and photon burst occurred at a high reactant concentration on the nanoamplifier with the thickest shell.

However, the ECL enhancement and accelerated photon emission on AuNR@mSiO$_2$ nanoamplifier are affected simultaneously by nanoconfinement and LSPR. To verify the critical function of the plasmonic AuNR core, nanoconfinement of mSiO$_2$ was separately investigated by completely removing the AuNR core (Figures 2d and S10). As shown in Figure 2a, the hollow mSiO$_2$ shells continued to play an effective role

***Table 1:*** Calculated values of reaction kinetics and equilibrium constants on different types of nanoamplifiers.

| Group | $k_{eff}$ ($s^{-1}$) | $K_{Ru}$ ($\mu M^{-1}$) |
|---|---|---|
| Thick AuNR@mSiO$_2$ | 7.0 ± 0.8 | 0.30 ± 0.07 |
| Medium AuNR@mSiO$_2$ | 5.3 ± 0.4 | 0.40 ± 0.09 |
| Thin AuNR@mSiO$_2$ | 4.0 ± 0.3 | 0.79 ± 0.10 |
| Thick mSiO$_2$ | 5.0 ± 0.5 | 0.38 ± 0.10 |
| Medium mSiO$_2$ | 3.7 ± 0.5 | 0.45 ± 0.10 |
| Thin mSiO$_2$ | 2.3 ± 0.2 | 0.53 ± 0.18 |

in increasing the ECL signal (enhancement ECL ratio from 3–10), but the effect was weaker than in the corresponding dual-function nanoamplifiers. Moreover, different particles with the same type of hollow mSiO$_2$ shell exhibited uniform enhancement ECL ratio compared with AuNR@mSiO$_2$. The nanoconfinement effect of mSiO$_2$ was derived from the mass transport ability of the mesopores. Reactive species after oxidation on the electrode accumulated inside the pores, resulting in frequent photon emissions.[30,41–43] Hence, the nanoconfinement effect totally disappeared when pores were occupied by surfactant (Figure S11). The adjustment of pore size also changed nanochannels and subsequently influenced enhancement ECL ratio, indicating another potential factor affecting nanoconfinement effect (Figure S12). The kinetics results demonstrated a discrepancy caused by the shell thickness, with the $k_{eff}$ value decreasing with decreasing mesopore nanospace (Figure 3a,b). However, the $K_{Ru}$ value did not substantially differ in the absence of the AuNR core, which may be attributed to a similar adsorption environment within the hollow silica shells. The ratio of $k_{eff}$ values before and after etching of the AuNR core suggested that molecules in the thin shell located near the plasmonic AuNR core tended to possess faster photon emission frequency than those in a thicker shell (Figure 3c). According to previous reports,[44,45] the photon emission of luminophores at intermediate distances (5–20 nm) can be enhanced by LSPR effects. The mesoporous shells could attenuate quenching phenomenon by spatially separating the luminophore from the plasmonic core. Given that emitters could diffuse into the mesopores, the shell thickness was not equivalent to the accurate distance from the plasmonic core.

Accordingly, the enhanced $k_{eff}$ value on a single nanoamplifier was attributed to the generation of hot spots due to LSPR effects. These hot spots principally relied on the oscillation of electrons of the metal surface and electric field enhancement.[46,47] Since this oscillation was triggered by ECL without an external light source, the overlap between Ru(bpy)$_3^{2+}$ emission and extinction of the nanoamplifier determined the plasmonic performance.[23,25,48] Hence, the AuNR aspect ratio was modified via controlled etching of the AuNR core without changing the shell structure (Figures 4a and S13). The aspect ratios of AuNR cores were tuned from 4:1 to 3:1 and finally to 2.25:1 relatively for analysis of LSPR effect while the shell thickness was uniformly maintained at 27.5 nm. The corresponding extinction and scattering peaks of AuNR@mSiO$_2$ shifted to the emission peak of Ru(bpy)$_3^{2+}$ with decreasing aspect ratio resulting in high spectral overlap (Figures 4b,c, and S14). Among these, the AuNRs with aspect

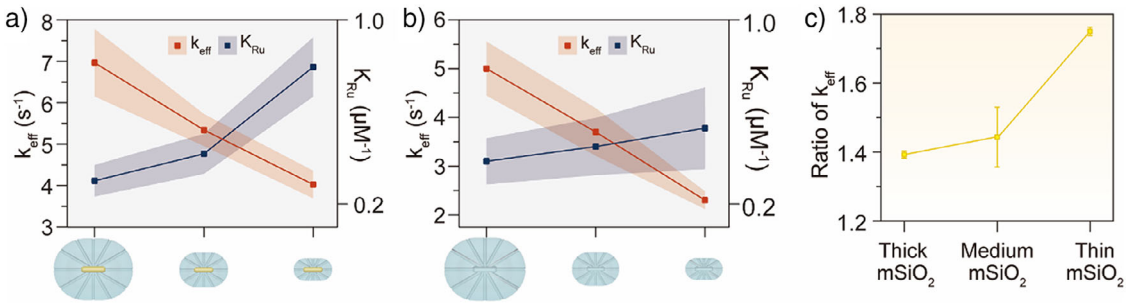


***Figure 3.*** a) Fitting results of $k_{eff}$ and $K_{Ru}$ values from TOF curves on AuNR@$mSiO_2$ nanoamplifiers with three different thicknesses (thick, medium, and thin shells from left to right). b) Fitting results of $k_{eff}$ and $K_{Ru}$ values from TOF curves on hollow silica shells (thick, medium, and thin shells from left to right). c) The ratio of $k_{eff}$ values before and after etching of the AuNR core. Error bars represent the standard error of fitting results.

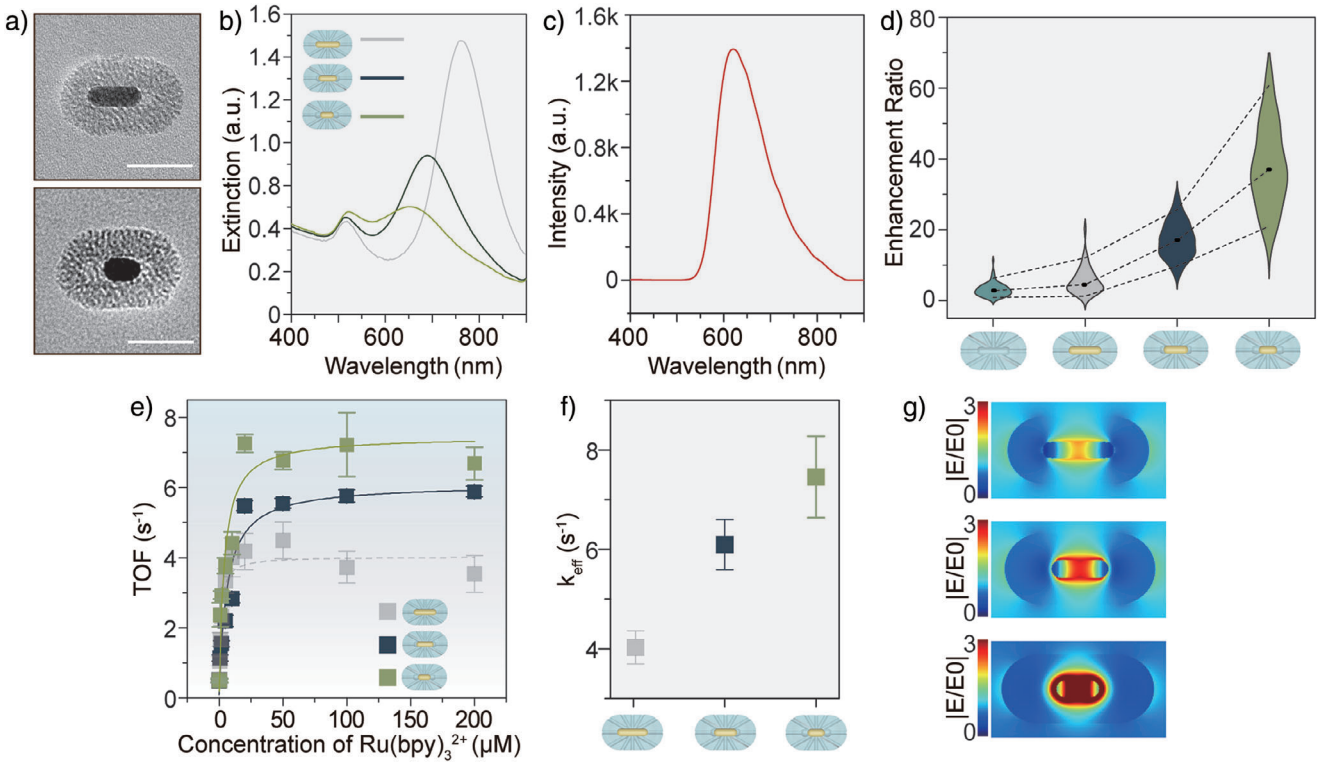


***Figure 4.*** a) TEM images of two kinds of nanoamplifiers after controllable etching of AuNR cores. Scale bar: 50 nm. b) Extinction spectrum of AuNR@$mSiO_2$ nanoamplifiers with AuNR cores of varying aspect ratio. c) PL spectrum of $Ru(bpy)_3^{2+}$ molecules. d) Enhancement ECL ratio on AuNR@$mSiO_2$ nanoamplifiers with AuNR cores of varying aspect ratio. e) TOF curves of three kinds of AuNR@$mSiO_2$ nanoamplifiers. Error bars represent the standard deviation ($n = 20$). f) $k_{eff}$ obtained by fitting with LH model. Error bars represent the standard error of fitting results. g) Simulation results of electric field enhancement on different nanoamplifiers. (Aspect ratio of AuNRs are 4:1, 3:1, 2.25:1 from top to bottom).

ratio of 2.25:1 exhibited an absorption peak at 650 nm, showing the closest spectral match to the $Ru(bpy)_3^{2+}$ emission peak. Although negligible in Figure 2a due to incomplete matching of the extinction spectrum, LSPR effect became obvious after etching of the AuNR core, and the enhancement ECL ratios were averaged 17 and 38, respectively (Figure 4d). The boost in ECL intensity essentially originated from the dramatically improved TOF and $k_{eff}$ values (Figure 4e,f). The $k_{eff}$ increased from 4.0 to 6.1 $s^{-1}$ and finally to 7.5 $s^{-1}$ with increasing spectral overlap. Moreover, plasmon resonance was identified as the dominant factor. In addition, simulation of the localized electric field confirmed that the proximity of the spectral peaks of nanoamplifier and $Ru(bpy)_3^{2+}$ led to stronger LSPR effects, which might result in the photon emission rate (Figure 4g).

Additionally, the plasmonic hot spots exhibited spatial heterogeneity along the nanostructures with distribution of enhanced electric field. The location of maximum enhancement of the electric field generally depended on the shape and size of nanoparticles.[5] Hence, AuNR@$mSiO_2$ with a high-aspect-ratio was prepared (Figures 5a, S15, and S16). The aspect ratio of AuNRs is 19:1 (375 × 20 nm) and the thickness of $mSiO_2$ shell is around 44 nm, which exhibited nanoconfinement to generate ECL photons and trigger LSPR

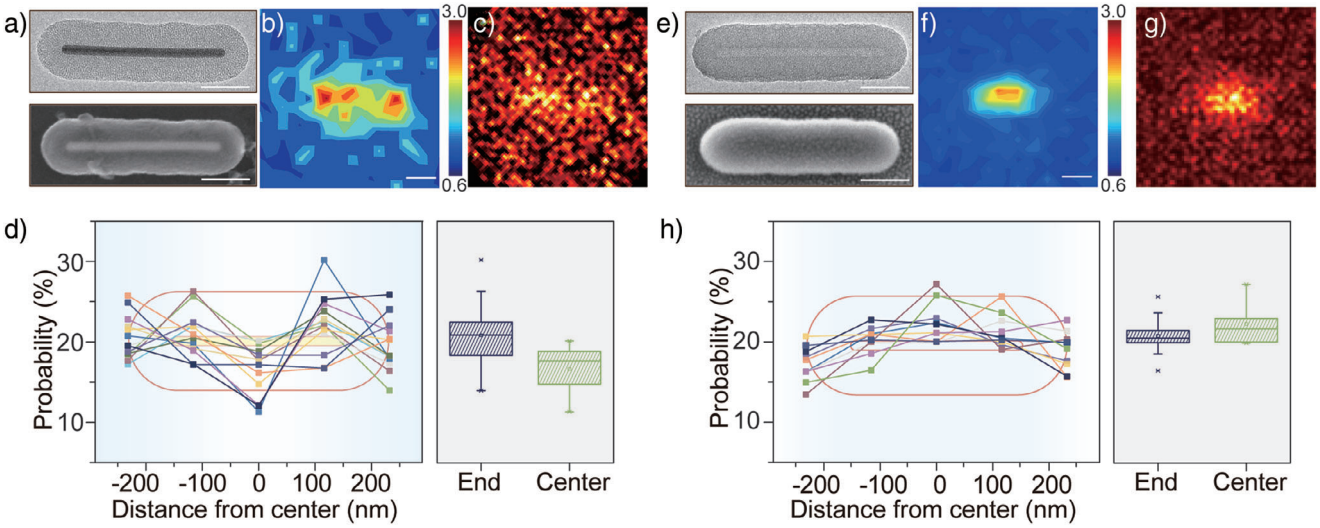


***Figure 5.*** a) TEM and SEM images of high-aspect-ratio AuNR@$mSiO_2$ (19:1). Scale bar: 100 nm. b) and c) TOF heatmap and super-resolution ECL images of AuNR@$mSiO_2$. Scale bar: 200 nm. d) The probability of photon emission at different segments of AuNR@$mSiO_2$. e) TEM and SEM images of high-aspect-ratio $mSiO_2$. Scale bar: 100 nm. f) and g) TOF heatmap and super-resolution ECL images of $mSiO_2$. Scale bar: 200 nm. h) The probability of photon emission at different segments of $mSiO_2$. The box plot displays the median, interquartile range, and maximum/minimum values for each group ($n = 20$).

effect. Single-particle dispersion of AuNR@$mSiO_2$ on the electrode (Figure S17) enabled us to map the accurate positions of photons by super-resolution ECL imaging and the obtained TOF distribution images of the nanoamplifier revealed a discrepancy along the nanostructures (Figures 5b and S18).[34] The TOF images demonstrated that photon emission hot spots always appeared at the extremities of AuNR@$mSiO_2$, reflecting the location of plasmonic hot spots (Figure S19), which aligned with the distribution of the enhanced electric field (Figure S20). In addition, the accurate positions of photons were extracted from super-resolution images and replotted to determine the probability distribution of molecular reaction collisions along the longitudinal AuNRs (Figures S21 and S22). Photons with relatively high density of photons appeared at both ends of the AuNR core, wherein the probability of photon emission increased (Figure 5c). By contrast, hot spots were not observed after etching the AuNR cores and the probability of photon emission showed no spatial distribution heterogeneity, indicating that the hot spots originated from the plasmonic effect (Figures 5d–f, S23 and S24).

Based on shell-isolated strategy and nanoconfined enhancement, it was also capable of unveiling the plasmonic performance and hot spot distribution of diverse nanostructures. Subsequently, AuNanowires and AuNanoplates were synthesized via step-wise seeded growth method to serve as plasmonic cores, which were then coated with a mesoporous silica shell to form AuNanowire@$mSiO_2$ and AuNanoplate@$mSiO_2$ nanostructures. The AuNanowires have an average length of 2.1 μm, enabling improved visualization of spatially dependent photon emission patterns (Figure S25). After complete etching, the hollow-shell nanostructure maintained structural stability and served as control. As shown in Figures 6a,b, S26, and S27, AuNanowire@$mSiO_2$ possessed higher reactivity than

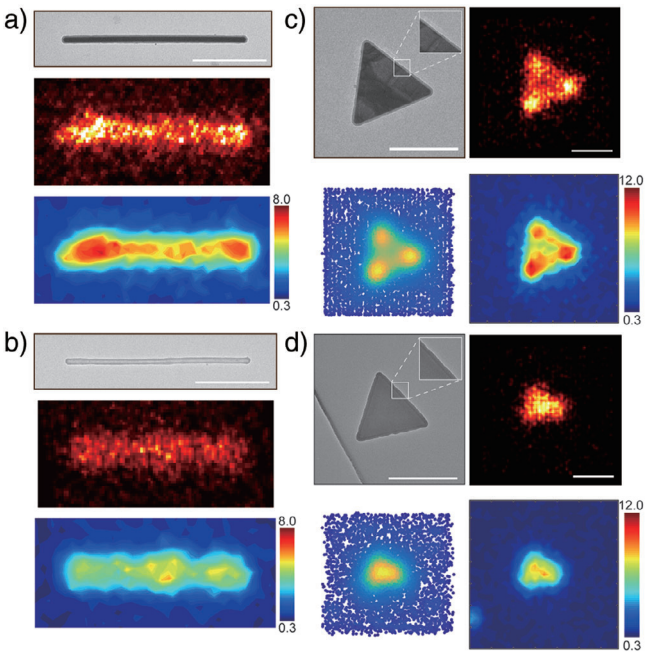


***Figure 6.*** a) and b) TEM images, super-resolution ECL images and TOF heatmaps of AuNanowire@$mSiO_2$ and related $mSiO_2$, respectively. Scale bar: 1 μm. c) and d) TEM images, super-resolution ECL images, photon mapping, and TOF heatmaps of AuNanoplate@$mSiO_2$ and related $mSiO_2$. Scale bar: 1 μm.

hollow $mSiO_2$ shell and displayed multiple hot spots along the nanostructure, especially at the ends. In addition, for AuNanoplate@$mSiO_2$, the average edge length is 0.88 μm and the maximum plasmonic reactivity appeared at the tip of the triangle structure, while $mSiO_2$ exhibited homogenous reactivity (Figures 6c,d, S28 and S30). The mesoporous shell

supplied a nanoconfined spaces to accommodate abundant reactive species and accelerate electrochemical reactions. Subsequently, the LSPR effect triggered by the enhanced ECL could be isolated and analyzed, and it induced a second burst of photon emissions at hot spots, which could be directly visualized.

## Conclusion

This approach based on single-molecule ECL microscopy provides an effective route to directly investigate both LSPR and nanoconfinement effects on core-shell plasmonic nanoamplifiers. Nonconductive mesoporous silica shells not only prevent electron transfer process between plasmonic core and electrode resulting in inhibition of electroactivity but also enable to accelerate ECL photons emission to effectively trigger LSPR effect due to nanoconfinement. Hence, for AuNR@m$SiO_2$ core-shell nanoamplifiers, regulation of the nanoconfined space and plasmonic properties can determine the final photon emissions to different degrees.

In addition, TOF images and super-resolution ECL analysis unveiled the plasmonic performance and hot spot distribution of diverse nanostructures including AuNR@m$SiO_2$, AuNanowire@m$SiO_2$, and AuNano-plate@m$SiO_2$. This strategy enables general hotspot characterization for plasmonic nanomaterials during electrochemical process. Hence, our study contributes to the comprehensive understanding of shell-isolated plasmonic nanomaterials during electrochemical reactions and offers insight for the design and fabrication of reasonable nanoarchitectures or plasmonic electrocatalysts.

## Acknowledgements

This work was supported by the National Key R&D Program of China (2022YFA1203400) and the National Natural Science Foundation of China (NSFC 22025403). N.S. acknowledges the financial support from ANR (MAPICS-ANR-23-CE42-0018-02), Grand Programme de Recherche LIGHT and European Union (MSCA ECLectic).

## Conflict of Interests

The authors declare no conflict of interest.

## Data Availability Statement

The data that support the findings of this study are available from the corresponding author upon reasonable request.

**Keywords:** Core-shell nanomaterials · Electrochemiluminescence imaging · Localized surface plasmon resonance

[1] X. Wang, S.-C. Huang, S. Hu, S. Yan, B. Ren, *Nat. Rev. Phys.* **2020**, *2*, 253–271.
[2] L. Mascaretti, A. Dutta, Š. Kment, V. M. Shalaev, A. Boltasseva, R. Zbořil, A. Naldoni, *Adv. Mater.* **2019**, *31*, 1805513.
[3] G. Tagliabue, J. S. DuChene, M. Abdellah, A. Habib, D. J. Gosztola, Y. Hattori, W. H. Cheng, K. Zheng, S. E. Canton, R. Sundararaman, J. Sa, H. A. Atwater, *Nat. Mater.* **2020**, *19*, 1312–1318.
[4] C. Wang, Y. Shi, D.-R. Yang, X.-H. Xia, *Curr. Opin. Electrochem.* **2018**, *7*, 95–102.
[5] Y. Wy, H. Jung, J. W. Hong, S. W. Han, *Acc. Chem. Res.* **2022**, *55*, 831–843.
[6] K. A. Willets, R. P. Van Duyne, *Annu. Rev. Phys. Chem.* **2007**, *58*, 267–297.
[7] C. Zhan, J. Yi, S. Hu, X.-G. Zhang, D.-Y. Wu, Z.-Q. Tian, *Nat. Rev. Methods Primers* **2023**, *3*, 12.
[8] E. Kazuma, J. Jung, H. Ueba, M. Trenary, Y. Kim, *Sicence* **2018**, *360*, 521–526.
[9] M. L. Brongersma, N. J. Halas, P. Nordlander, *Nat. Nanotechnol.* **2015**, *10*, 25–34.
[10] J. Zhao, S. Xue, R. Ji, B. Li, J. Li, *Chem. Soc. Rev.* **2021**, *50*, 12070–12097.
[11] B. S. Hoener, S. R. Kirchner, T. S. Heiderscheit, S. S. E. Collins, W.-S. Chang, S. Link, C. F. Landes, *Chem* **2018**, *4*, 1560–1585.
[12] Y. Leroux, J. C. Lacroix, C. Fave, V. Stockhausen, N. Félidj, J. Grand, A. Hohenau, J. R. Krenn, *Nano Lett.* **2009**, *9*, 2144–2148.
[13] S. Ganguli, Z. Zhao, O. Parlak, Y. Hattori, J. Sa, A. Sekretareva, *Angew. Chem. Int. Ed.* **2023**, *62*, e202302394.
[14] S. S. Wang, L. Jiao, Y. Qian, W. C. Hu, G. Y. Xu, C. Wang, H. L. Jiang, *Angew. Chem. Int. Ed.* **2019**, *58*, 10713–10717.
[15] W. Zhang, J. Li, X. H. Xia, Y. G. Zhou, *Angew. Chem. Int. Ed.* **2022**, *61*, e202115819.
[16] S. Knezevic, D. Han, B. Liu, D. Jiang, N. Sojic, *Angew. Chem. Int. Ed.* **2024**, *63*, e202407588.
[17] J. Dong, J. Feng, *Anal. Chem.* **2023**, *95*, 374–387.
[18] W. Zhao, H.-Y. Chen, J.-J. Xu, *Chem. Sci.* **2021**, *12*, 5720–5736.
[19] S. Knezevic, L. Bouffier, B. Liu, D. Jiang, N. Sojic, *Curr. Opin. Electrochem.* **2022**, *35*, 101096.
[20] J. Dong, Y. Xu, Z. Zhang, J. Feng, *Angew. Chem. Int. Ed.* **2022**, *134*, e202200187.
[21] M. M. Chen, C. H. Xu, W. Zhao, H. Y. Chen, J. J. Xu, *J. Am. Chem. Soc.* **2021**, *143*, 18511–18518.
[22] M. M. Chen, W. Zhao, M. J. Zhu, X. L. Li, C. H. Xu, H. Y. Chen, J. J. Xu, *Chem. Sci.* **2019**, *10*, 4141–4147.
[23] Y. Wei, Y. Zhang, J. Pan, T. Chen, X. Xing, W. Zhang, Z. Lu, *Angew. Chem. Int. Ed.* **2022**, *62*, e202214103.
[24] S. Pan, J. Liu, C. M. Hill, *J. Phys. Chem. C* **2015**, *119*, 27095–27103.
[25] T. S. Heiderscheit, S. Oikawa, S. Sanders, H. Minamimoto, E. K. Searles, C. F. Landes, K. Murakoshi, A. Manjavacas, S. Link, *J. Phys. Chem. Lett.* **2021**, *12*, 2516–2522.
[26] M. P. Dinel, S. Tartaggia, G. Q. Wallace, D. Boudreau, J. F. Masson, F. Polo, *Angew. Chem. Int. Ed.* **2019**, *58*, 18202–18206.
[27] M. M. Chen, C. H. Xu, W. Zhao, H. Y. Chen, J. J. Xu, *Chem. Commun.* **2020**, *56*, 3413–3416.
[28] M. J. Zhu, J. B. Pan, Z. Q. Wu, X. Y. Gao, W. Zhao, X. H. Xia, J. J. Xu, H. Y. Chen, *Angew. Chem. Int. Ed.* **2018**, *57*, 4010–4014.
[29] Q.-Q. Tao, C.-H. Xu, W. Zhao, H.-Y. Chen, J.-J. Xu, *Chem. Commun.* **2024**, *60*, 2520–2523.
[30] X. Huang, B. Li, Y. Lu, Y. Liu, S. Wang, N. Sojic, D. Jiang, B. Liu, *Angew. Chem. Int. Ed.* **2023**, *62*, e202215078.
[31] J. Wordsworth, T. M. Benedetti, S. V. Somerville, W. Schuhmann, R. D. Tilley, J. J. Gooding, *Angew. Chem. Int. Ed.* **2022**, *61*, e202200755.

[32] Y. Lu, X. Huang, S. Wang, B. Li, B. Liu, *ACS Nano* **2023**, *17*, 3809–3817.
[33] Y. Liu, H. Zhang, B. Li, J. Liu, D. Jiang, B. Liu, N. Sojic, *J. Am. Chem. Soc.* **2021**, *143*, 17910–17914.
[34] J. Dong, Y. Lu, Y. Xu, F. Chen, J. Yang, Y. Chen, J. Feng, *Nature* **2021**, *596*, 244–249.
[35] Z. Zhang, J. Dong, Y. Yang, Y. Zhou, Y. Chen, Y. Xu, J. Feng, *Nat. Commun.* **2023**, *14*, 7993.
[36] V. Pellas, J. Blanchard, C. Guibert, J.-M. Krafft, A. Miche, M. Salmain, S. Boujday, *ACS Appl. Nano Mater.* **2021**, *4*, 9842–9854.
[37] W. C. Wu, J. B. Tracy, *Chem. Mater.* **2015**, *27*, 2888–2894.
[38] L. Zhang, K. Xia, Z. Lu, G. Li, J. Chen, Y. Deng, S. Li, F. Zhou, N. He, *Chem. Mater.* **2014**, *26*, 1794–1798.
[39] X. Zhou, N. M. Andoy, G. Liu, E. Choudhary, K. S. Han, H. Shen, P. Chen, *Nat. Nanotechnol.* **2012**, *7*, 237–241.
[40] B. Dong, Y. Pei, F. Zhao, T. W. Goh, Z. Qi, C. Xiao, K. Chen, W. Huang, N. Fang, *Nat. Catal.* **2018**, *1*, 135–140.
[41] B. Li, X. Huang, Y. Lu, Z. Fan, B. Li, D. Jiang, N. Sojic, B. Liu, *Adv. Sci.* **2022**, *9*, 2204715.
[42] Z. Xing, X. Gou, L. P. Jiang, J. J. Zhu, C. Ma, *Angew. Chem. Int. Ed.* **2023**, *62*, e202308950.
[43] B. Li, Y. Lu, X. Huang, N. Sojic, D. Jiang, B. Liu, *Angew. Chem. Int. Ed.* **2025**, *64*, e202421658.
[44] L. H. Lin, J. Y. Wang, C. Y. You, L. H. Qiu, J. S. Lin, F. L. Zhang, Z. L. Yang, Y. J. Zhang, X. Chen, J. F. Li, *Small* **2022**, *18*, 2203513.
[45] D. Wang, L. Guo, R. Huang, B. Qiu, Z. Lin, G. Chen, *Sci. Rep.* **2015**, *5*, 7954.
[46] C. Ma, Z. Zhang, T. Tan, J.-J. Zhu, *Biosensors* **2023**, *13*, 200.
[47] J. Zhang, Z. Gryczynski, J. R. Lakowicz, *Chem. Phys. Lett.* **2004**, *393*, 483–487.
[48] T. S. Heiderscheit, M. J. Gallagher, R. Baiyasi, S. S. E. Collins, S. A. Hosseini Jebeli, L. Scarabelli, A. Al-Zubeidi, C. Flatebo, W. S. Chang, C. F. Landes, S. Link, *J. Chem. Phys.* **2019**, *151*, 144712.

Manuscript received: April 14, 2025
Revised manuscript received: June 30, 2025
Accepted manuscript online: July 01, 2025
Version of record online: July 16, 2025